Title
Structural evaluation of axial and rotational flexibility and strength of web-flange junctions of open-web pultruded composites

Journal
Composites Part B: Engineering, 66

ISSN
1359-8368

Authors
Mosallam, AS
Feo, L
Elsadek, A
et al.

Publication Date
2014

DOI
10.1016/j.compositesb.2014.05.018

Peer reviewed

Composites: Part B 66 (2014) 311–327

Contents lists available at ScienceDirect

Composites: Part B

journal homepage: www.elsevier.com/locate/compositesb

Structural evaluation of axial and rotational flexibility and strength of web–flange junctions of open-web pultruded composites

A.S. Mosallam [a], L. Feo [b], A. Elsadek [a], S. Pul [c], R. Penna [b,*]

[a] Dept. of Civil & Env. Engineering, University of California, Irvine, 92697 CA, USA
[b] Department of Civil Engineering, University of Salerno, 84084 Fisciano, SA, Italy
[c] Dept. of Civil Engineering, Karadeniz Technical University, 61080 Trabzon, Turkey

ARTICLE INFO

Article history:
Received 27 January 2014
Received in revised form 9 May 2014
Accepted 15 May 2014
Available online 27 May 2014

Keywords:
A. Polymer–matrix composites (PMCs)
B. Delamination
B. Strength
D. Mechanical testing

ABSTRACT

In past few decades, the interest in using pultruded fiber reinforced polymeric (PFRP) composites in construction applications has grown rapidly. Several research studies were conducted and focused on the performance of PFRP beams, columns and frame structures. The results of the majority of previous studies highlighted a major problem associated with the deficiency of the off-the-shelf, unidirectional open-web pultruded profiles. In this regards, a common conclusion was drawn by many researchers; that is: the inherent structural deficiency of commercially produced unidirectional PFRP profiles, especially at the flange/web(s) junction(s) that lacks fiber continuity. The lack of fiber continuity creates a "resin-rich" zones at the junctions that were shown to be responsible for rapid degradation of both axial and rotational stiffness as well as the strength of the majority of PFRP profiles. Another related problem is the use of incorrect framing connection details, currently being used by industry.

Such connection details mimic those associated with steel structures. This approach ignores both the anisotropic and the viscoelastic nature of composites as well as the aforementioned inherent junction deficiency that, in most cases, lead to a greater risk with regard to the safety, reliability and economic aspects of such structures. This paper presents a summary of an experimental study aimed at evaluating both axial and rotational stiffnesses and strengths of web–flange junctions, which may affect stiffness, buckling, post-buckling, torsional and overall strength of PFRP structures. In particular, three sizes of commercially-produced unidirectional pultruded H-profiles and two sizes of L-profiles were evaluated under both service and ultimate loads. Using full-scale experimental data, P–δ and M–θ relations and idealized expressions for each pultruded profile were developed that can be used for accurate modeling and for establishing design limit-states for PFRP structures. In addition, two special test fixtures were designed, fabricated and validated that can be adopted by ASTM/ISO standards for characterizing such critical mechanical properties that are essential for reliable design of pultruded composite structures. Conclusions and design recommendations are also presented.

1. Introduction

Fiber-reinforced polymers (FRP) represent a relatively new class of construction materials. In the past two decades or so, their use has spread from the aerospace industry to civil infrastructure, which has generated a new set of challenges. During last few decades, pultruded fiber reinforced polymer (PFRP) composites have been used in corrosive environments including cooling towers, mining and petrochemical facilities, water and wastewater treatment plants, as well as, off-shore structures. By mid-1990s, major applications of the use of FRP composites were reported, especially in the area of seismic and corrosion repair and rehabilitation of existing reinforced concrete bridges and buildings. This application was extended to cover strengthening of other structures made of timber, masonry and steel.

Historically, the majority of commercially-produced PFRP composites were designed and developed by the industry and were intended for low-stress applications such as ladders, cat-walks, stair rails, and cable trays. With the demand of exploring new alternative construction materials in early 1990, composites have been introduced as primary structural members to replace some of the conventional materials, such as steel and concrete, in critical applications such as bridge decks, pedestrian bridges, and recently

* Corresponding author. Tel.: +39 089964096.
E-mail address: rpenna@unisa.it (R. Penna).

http://dx.doi.org/10.1016/j.compositesb.2014.05.018
1359-8368/

in highway bridges and other infrastructural systems [1,2]. Unfortunately, no major engineering design modifications to the original PFRP profile that were intended for secondary structural applications, were made prior to introducing such materials for high-stress structural members. This results in several unsuccessful applications such those reported by Mosallam [3,4].

PFRP composites are commercially-produced in a number of different "steel-like" profiles including H-, I-, L- and tubular profiles. In order to make pultruded members appealing to the construction industry that have limited knowledge on the special characteristics of polymer composites such as anisotropy and viscoelastic behaviors, most pultruders produce profiles that imitate traditional structural steel members, even though these profiles do not represent the optimum geometry for PFRP material, as will be described in this paper. On the positive side, composites offer unique features, when designed, fabricated and installed correctly that include high strength-to-weight ratio, durability, damping capabilities, toughness, electromagnetic transparency, and other characteristics that beneficial to different construction applications.

As mentioned earlier, and unlike isotropic, time-independent structural materials such as steel, all PFRP composites are anisotropic and are characterized as viscoelastic materials [5–7]. Their stiffness and strengths have values that depend on the orientation of the fibers in the beam cross section. Consequently, these materials behave differently from those isotropic time-independent structural materials such as steel, under service, ultimate loads and dynamic excitations.

In order to ensure the structural reliability of load bearing pultruded composite members, the shape and fiber architecture of PFRP profiles must be optimized and designed properly. Standard engineering guidelines, analytical and design tools developed for conventional materials are not applicable to FRP shapes. For this reason, several technical documents dealing with design equations and methods, material properties and safety factors for pultruded elements have been or being developed in recent years [8–12].

On the other hand, finite element analysis (FEA) and other numerical methods, which could provide more accurate results require specialized training, utilize complicated modeling, and are not always accessible to design engineers. In addition, the majority of commercial FEA codes will need to be adjusted to include some specific characteristics and deficiencies of the materials. For example, most of the FEA codes are developed for laminated composites with no attention to the inherent problems associated with pultruded composite such as the deficiency of the web–flange junction that impacts the analysis of joints, buckling and post-buckling of PFRP members and the rotational flexibility of the framing connections such as beam-column, beam-girder and column-base connections. For these reasons, FEA codes must be supplemented with experimental or semi-empirical equations to truly capture these specific features of PFRP materials and structures. This important issue has been discussed in depth in Chapter 9 of the American Society of Civil Engineers (ASCE) Manual of Practice (MOP) 102 [11].

Therefore, in order to safely expand the structural applications of pultruded composites, a comprehensive design methodology should be developed and made accessible to practitioners, so that they may confidently perform an analysis on standard and unique PFRP structures.

In recent years, several programs on optimizing pultruded composites have been initiated. For example Davalos et al. [13] presented an approach for flexural analysis and design of pultruded beams. This approach involved computational procedures for utilizing fiber volume fraction of the constituents, ply stiffness and panel laminate engineering constants. Over the past two decades or so, a number of studies focusing on the performance of PFRP connections and frame structures have also been reported. Some of the pioneering studies on PFRP frame structures were reported by Mosallam et al. [14–17] presenting the results of a comprehensive theoretical and experimental program to evaluate both the short- and long-term behavior of PFRP structures subjected to both quasi-static and sustained loading.

A highly complex and delicate mechanical aspect unique to steel-like unidirectional PFRP profiles is associated with the strength and stiffness of web–flange junctions (WFJ) of such profiles due to the insufficient fiber continuity. This insufficient fiber continuity will lead to progressive degradations of both axial and rotational stiffnesses and strengths affecting buckling, post-buckling and the overall short- and long-term structural integrity of the PFRP structures [18–22]. Some relevant studies related to this topic have been also proposed by Turvey and Zhang [23–25] and Borowicz and Bank [26]. Due to the critical impact of the web–flange junction local failure on the structural behavior of pultruded composites that are being currently used by the construction industry, it is necessary to develop techniques to detect such type of potential localized failure. Leung et al. [27] developed a fiber optic based technique to detect delamination at the web/flange junction of a GFRP I-beam.

2. Motivations and merits

This paper presents the results of a second phase of a multi-phase comprehensive joint research program between University of Salerno, Italy, and the University of California, Irvine, USA, with appreciable contributions in developing the test fixtures from Karadeniz Technical University, Trabzon, Turkey. The results of the first phase of this joint research, conducted at the Materials and Structural Testing Laboratory (LMS) of the Department of Civil Engineering of the University of Salerno in order to develop the junction P–δ relation and stiffness expressions of I-profiles, have been already presented by and Feo et al. [28]. The experimental investigation carried out in the second part of this joint research focuses on the evaluation of both the axial and rotational stiffnesses of WFJ of H- and L-profiles tested under both service and ultimate load and was conducted at the Structural Engineering Test Hall (SETH), an ISO-17025 accredit facility, at the University of California, Irvine (UCI). In particular, load–displacement (P–δ) and moment–rotation (M–θ) relations have been developed in order to accurately model and in order to establish design limit-state of PFRP structures, necessary to predict the local and global responses of PFRP structures [27–32]. In addition, these expression can also be integrated in different commercial FEA codes to simulate accurate behavior of PFRP structures.

The results of the current pilot study provides much needed information that will allow structural engineers to understand the limitations of these systems and help to produce safe designs for such structures. Unlike the majority of published research in the field of PFRP frame connections, this study examines several critical parameters that are commonly ignored. These parameters include axial and rotational flexibility of the web/flange junction of open-web thin-walled profile which play a major role on buckling and post-buckling behavior of such frames and, also, limit both the strength and stiffness of PFRP structural members. To date, the majority of published work focused in analyzing and experimentally evaluating PFRP frame structures with deficient "steel-like" connection details resulting in premature failure and offering minimum benefit to the engineering knowledge.

3. PFRP frame connections

The efficiency of beam-column connections are one of primary concern to structural engineers. These connections are designed to

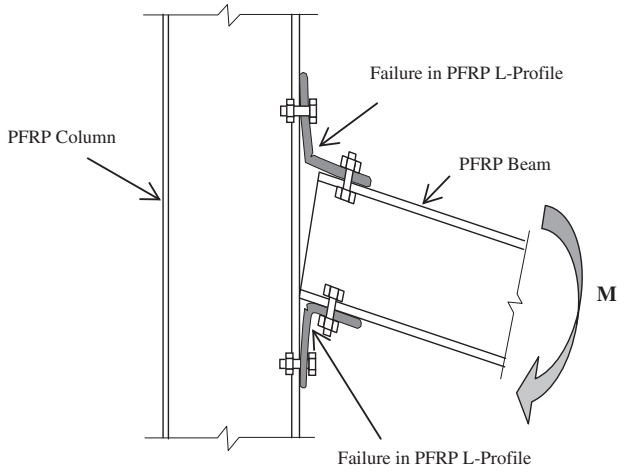

Fig. 1. Typical failure of composite cleat connections.

transfer moments, shear, axial forces and any other loads. Fig. 1 shows a typical failure of a bolted FRP beam-column connection in which angle sections are used to join the flanges of a beam and a column [11].

The FRP angle fails by the formation of hinges, due to opening (top) or closing (bottom) moments. Other likely locations of failure are under the bolts going through the column (crushing) and at the junction of web and flange of FRP I-beams, which is an area that is relatively rich in resin and poor in fibers (matrix-dominated), as shown in Fig. 2 [11,15].

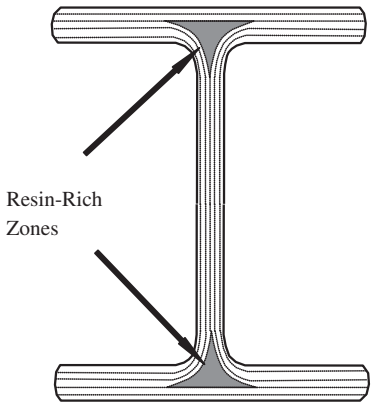

Fig. 2. Resin (matrix)-rich zones at web/flange junction of unidirectional pultruded profiles.

4. Experimental setup

The test program was conducted at the Structural Engineering Testing Hall (SETH) of the University of California Irvine (UCI) and consisted of two parts: the first one was an evaluation of the axial behavior for web–flange junction of PFRP E-glass/polyester H-profiles (pull-out tests), while the second part was an evaluation of the relative rotational behavior of the web/flange junctions of PFRP E-glass/polyester H- and L-profiles (relative rotation tests).

The geometrical characteristics of the PFRP profiles evaluated in this paper are presented in Table 1. The nominal values of the main mechanical properties for the pultruded shapes were recommended by the manufacture (Bedford Reinforced Plastics [33]) and are summarized in Table 2.

4.1. Pull-out test setup and instrumentation

For pull-out tests, a total of six specimens, cut from commercially-produced structural PFRP H-profiles and characterized by three different sizes, i.e. 10″ × 10″ × ½″ (254 mm × 254 mm × 12.7 mm), 8″ × 8″ × 3/8″ (203.2 mm × 203.2 mm × 9.53 mm) and 6″ × 6″ × 3/8″ (152.4 mm × 152.4 mm × 9.53 mm), were evaluated (Table 1). The length (l) of the specimens was equal to 24 in. (609.6 mm).

In particular, two different test setups were carried out, varying the location of the pull-out force. The first test setup (*Group 1* of specimens), the load was applied at the mid-point (*MP*) of the specimens, i.e. at a distance of $l/2$ from the edge of the specimen as shown in Fig. 3a simulating cases of local buckling of a beam or a column similar to those reported by Mosallam and Bank [16]

Table 2
Mechanical properties for pultruded structural shapes (nominal values).

Property	Measurement unit	Value
Tensile strength		
Lengthwise	psi (MPa)	30,000 (206.80)
Crosswise	psi (MPa)	6500 (44.80)
Tensile modulus		
Lengthwise	psi × 10^6 (GPa)	2.3 (15.85)
Crosswise	psi × 10^6 (GPa)	0.8 (5.51)
Flexural strength		
Lengthwise	psi (MPa)	30,000 (206.80)
Crosswise	psi (MPa)	10,000 (68.93)
Flexural modulus		
Lengthwise	psi × 10^6 (GPa)	1.5 (10.30)
Crosswise	psi × 10^6 (GPa)	0.7 (4.80)
Compressive strength		
Lengthwise	psi (MPa)	30,000 (206,80)
Crosswise	psi (MPa)	10,000 (68.93)

Table 1
Geometry of the pultruded profiles.

Specimen type		Web length H in. (mm)	Flange length W in. (mm)	Web and flange thickness t in. (mm)
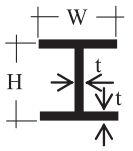	H_10″ × 10″ × ½″	10 [254.0]	10 [254.0]	½ [12.7]
	H_8″ × 8″ × 3/8″	8 [203.2]	8 [203.2]	3/8 [9.53]
	H_6″ × 6″ × 3/8″	6 [152.4]	6 [152.4]	3/8 [9.53]
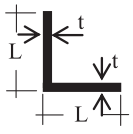	L_6″ × 6″ × ½″	6 [152.4]	6 [152.4]	½ [12.7]
	L_4″ × 4″ × 3/8″	4 [101.6]	4 [101.6]	3/8 [9.53]

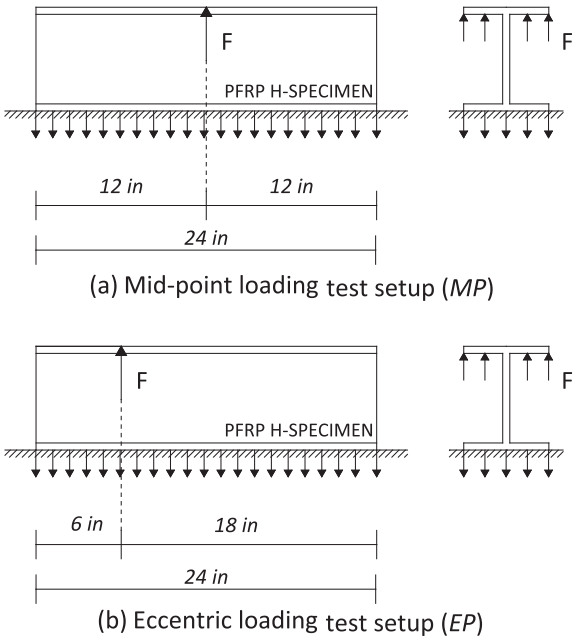

Fig. 3. (a, b) Schematic setup of web–flange junction pullout test.

and by Hassan and Mosallam [34] as shown in Fig. 4a. The second test setup (*Group 2* of specimens), the load was eccentrically applied (*EP*) at a distance of *l*/*4* from the edge of the specimen as shown in Fig. 3b simulating the typical failure of open-web pultruded columns at the beam-column framing connections similar to those reported by Mosallam [11] and shown in Fig. 4b.

For all specimens, the pull axial load was applied using a calibrated MTS 55-kip (245 kN) servo-hydraulic actuator. Two rigid steel angles were used to provide fixity to the lower flange and web of PFRP H-profiles. A force-controlled loading protocol was adopted in all tests. Figs. 5 and 6 show schematic diagram and photos of the pullout test setup, respectively. These two sets of tests were performed using especially-designed steel fixture (Fig. 6) that was mounted to the 55-kip (245 kN) calibrated hydraulic actuator. In designing this special test fixture, several requirements were considered including: (i) producing even loading on the two overhang portions of the flange, (ii) avoiding edge stress concentration, (iii) providing simplicity and (iv) considering economic aspects for potential future adoption by ASTM/ISO for establishing stand-alone standard test procedures.

In order to capture web displacements, five calibrated string potentiometers were used and placed at each side of specimen, at 6″ (152.40 mm) distances as shown in Fig. 7. Moreover, two strain gauges were used to measure the strain at the web/flange junction (Fig. 7). A calibrated computerized data acquisition

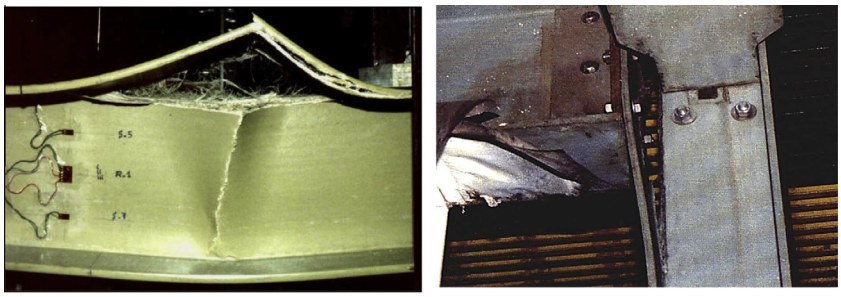

Fig. 4. (a, b) Typical mode of localized web/flange failure: (a) local buckling; (b) flange separation at connection zone.

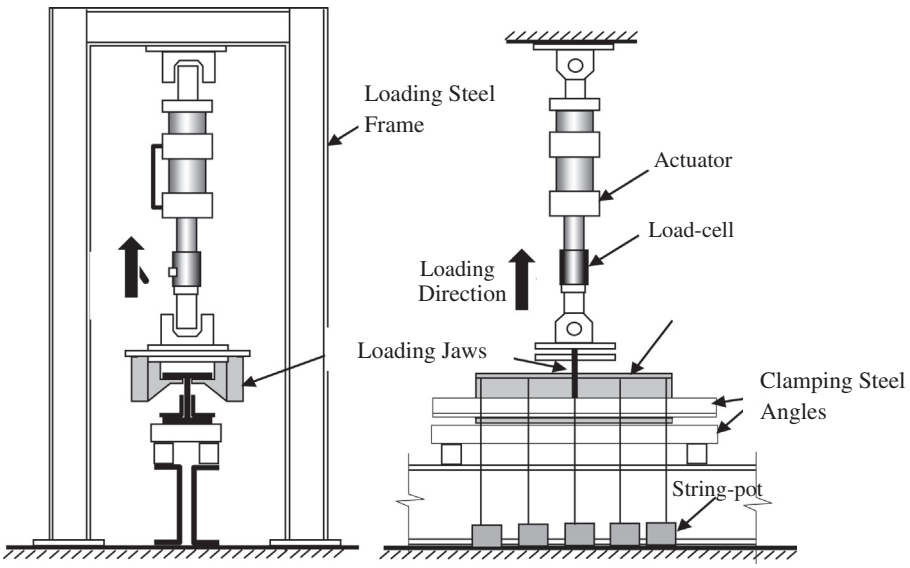

Fig. 5. Schematic views of pull-out test setup.

Fig. 6. Typical pull-out web/flange test setup.

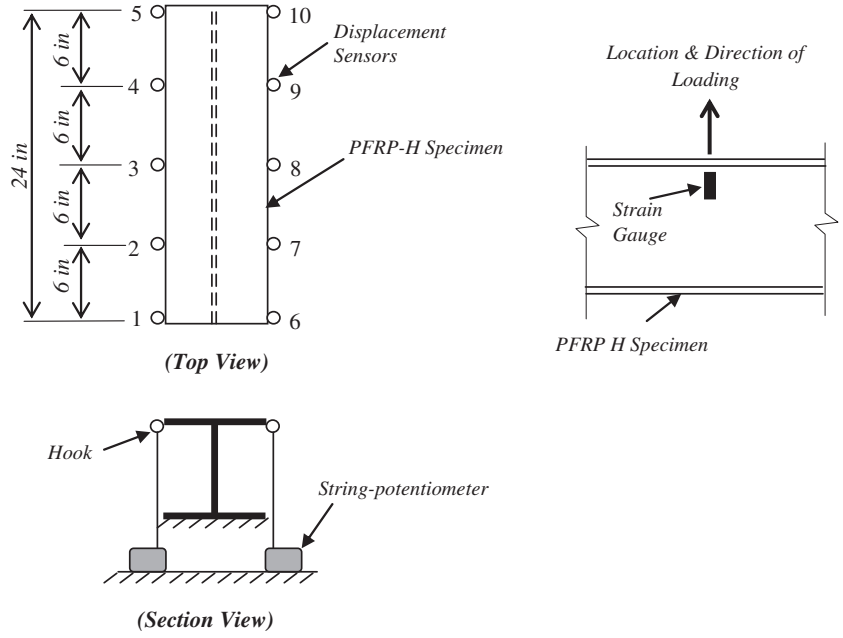

Fig. 7. Locations of string-potentiometers and strain gauges.

system was used to continuously collect load, displacement, and strain experimental data.

4.2. Relative rotation test setup and instrumentation

4.2.1. Development of special test fixture for rotational stiffness and strength of web/flange junctions

Due to the critical need for characterizing the relative rotation stiffness and strength of pultruded open-web profile in accurately predict and analyze the behavior of such members at both buckling and post-buckling stages, a reliable test fixture and procedure are required. For this reason, a special steel mechanism was developed to simulate such actions. The proposed web/flange rotation test fixture is illustrated in Fig. 8.

In order to generate the desired behavior, specimens were securely held at the lower flange and web, while rotation was applied to the upper flange. Fig. 9 shows a schematic for the flange/web relative rotation test. For all tests, moment was applied over the 6″ (152.40 mm) length profiles.

4.2.2. Web/flange junctions relative rotation test matrix

For relative rotation characterization tests, three sizes of off-the-shelf unidirectional E-glass/polyester pultruded H-profiles were evaluated. The three PFRP profiles are (i) 10″ × 10″ × ½″ (254 × 254 × 12.70 mm), (ii) 8″ × 8″ × 3/8″ (203.20 × 203.20 × 9.53 mm) and (iii) 6″ × 6″ × 3/8″ (152.40 × 152.40 × 9.53 mm). In addition, two sizes of E-glass/polyester pultruded L-profiles were also evaluated. The pultruded equal-leg angles assessed in this phase are: (i) 6″ × 6″ × ½″ (152.4 × 152.4 × 12.7 mm) and (ii) 4″ × 4″ × 3/8″ (101.60 × 101.60 × 9.53 mm). The importance of evaluated the pultruded angles is due to the potential localized failure at the legs junction that have been observed both at the laboratory tests as well as in the field applications reported by Mosallam et al. [14] and by Mosallam [3] as shown in Figs. 10 and 11, respectively. Table 1 presents a summary of the specimens assessed in this study. It should be noted that for all specimens, the length (l) of the specimens was equal to 24″ (609.60 mm).

In all tests, moment was applied via an eccentric axial load through a calibrated MTS 55-kip (245 kN) servo-hydraulic

Fig. 8. Views from rotation test setup.

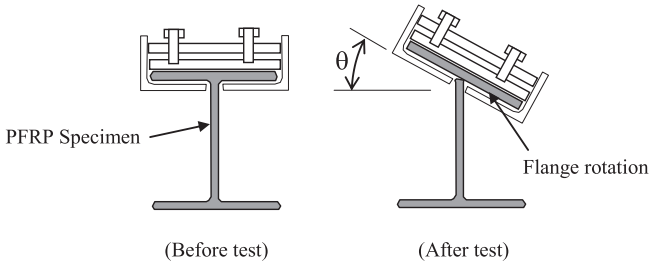

Fig. 9. Schematic view of flange rotation.

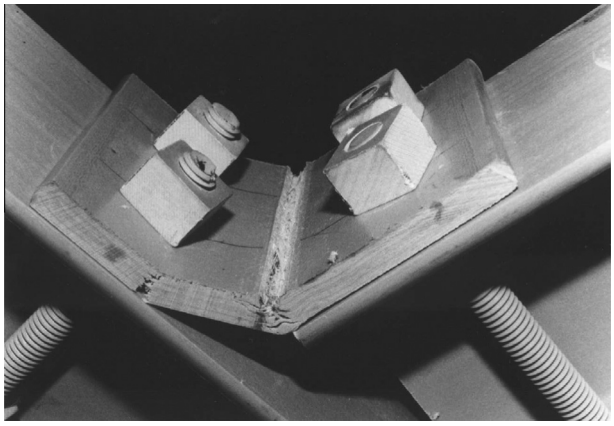

Fig. 10. Localized failure of unidirectional pultruded angle.

actuator. Two thick steel angles were used to provide fixity to the lower flange and web of the PFRP H-profiles. The displacement-controlled protocol was adopted in all tests. Fig. 12 shows a schematic diagram of rotation test setup.

Two measurement methods were used to capture the web/flange relative rotation characteristics. In the first method, two calibrated string potentiometers were used and placed at each side of specimen as shown in Fig. 8 to capture the relative displacement between the two edges of the upper flange in order to calculate the rotation angle. While, in the second method, two calibrated inclinometers were used to capture the rotation angle. In addition, two strain gauges were used to measure strain at the web/flange junction as shown in Fig. 8. A calibrated computerized data-acquisition system was used to continuously collect all information including load, displacement, rotation angle and strain.

5. Experimental results

5.1. Pullout test results

As described earlier, two sets of pullout tests were employed to simulate the following potential loading scenarios:

(i) Case of buckling and post-buckling at maximum compressive zone (Fig. 4a) of a beam or a column that is simulated by a mid-point pull loading (Fig. 3a).
(ii) Case of beam/column connections (Fig. 4b) that is simulated by an edge or eccentric loading (Fig. 3b).

The main experimental results obtained from the pullout tests are summarized in Tables 3 and 4. In the last two columns of these tables, two proposed values for junction's linear stiffness are presented (Fig. 13) and namely, the linear axial stiffness K_{jl}^{A}, and the average linear axial stiffness $\bar{K}_{jl}^{A}$ (Feo et al. [28]). Figs. 14 and 15 present the load versus displacement curves for the H-specimens in mid-point loading and for the H-profiles in eccentric-point loading, respectively.

In the following paragraphs, load–displacement curves at loading-point and the corresponding equivalent linearized relations P–δ for all the specimens are presented.

5.1.1. Group 1: Mid-point loading tests results

– *Specimen #1* H_10″ × 10″ × ½″ (254.0 mm × 254.0 mm × 12.7 mm)_*MP*.

For this specimen, the displacement increased linearly with increasing load up to an axial displacement of 0.26″ (6.60 mm) that

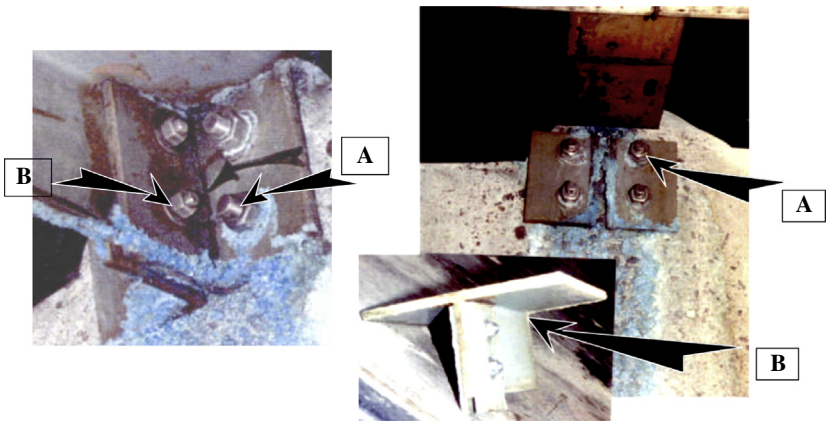

Fig. 11. Failure of unidirectional pultruded angle at a mining facility structure.

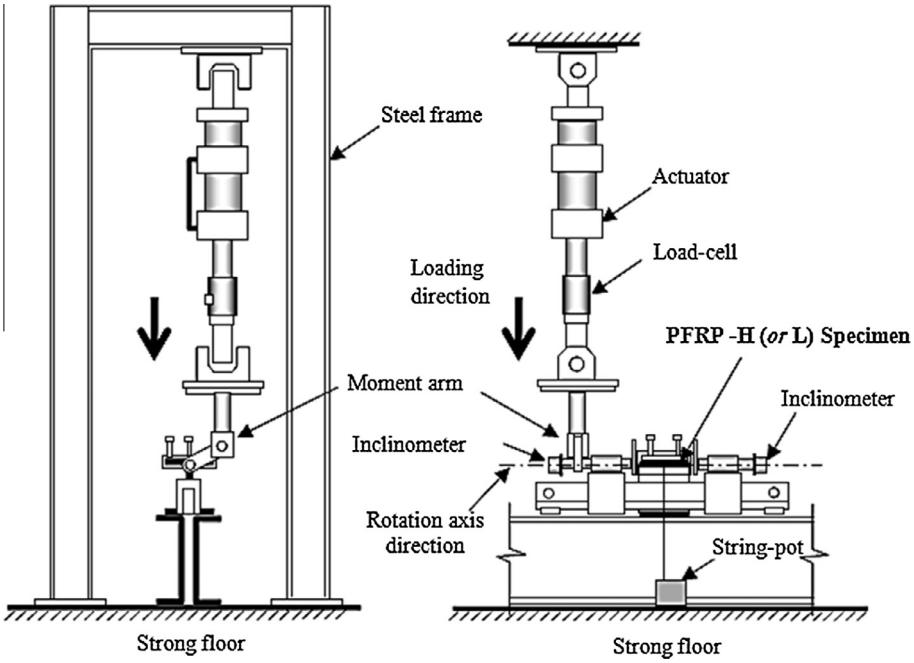

Fig. 12. Schematic views of rotation test setup.

Table 3a
Experimental results for specimens of *Group 1* (H-specimens in mid-point loading): failure loads, displacements and linear axial stiffnesses (values in kips, in.).

#	Specimens	Length (in.)	Load (linear limit) (P_l) (kips)	δ_l (in.)	Failure load (P_f) (kips)	δ_f (in.)	Linear axial stiffness K_{jl}^A (kip/in)	Average lin. axial stiffness $\overline{K}_{jl}^A$ (kip/in)
1	H_10″ × 10″ × 1/2″_*MP*	24	4.25	0.26	5.43	0.56	16.40	12.40
2	H_8″ × 8″ × 3/8″_*MP*	24	3.58	0.20	3.58	0.20	19.16	–
3	H_6″ × 6″ × 3/8″_*MP*	24	2.46	0.13	3.14	0.20	20.42	17.66

Table 3b
Experimental results for specimens of *Group 1* (H-specimens in mid-point loading): failure loads, displacements and linear axial stiffnesses (values in kN, mm).

#	Specimens	Length (mm)	Load (linear limit) (P_l) (kN)	δ_l (mm)	Failure load (P_f) (kN)	δ_f (mm)	Linear axial stiffness K_{jl}^A (kN/mm)	Average lin. axial stiffness $\overline{K}_{jl}^A$ (kN/mm)
1	H_10″ × 10″ × 1/2″_*MP*	609.6	18.93	6.60	24.15	14.22	2.87	2.17
2	H_8″ × 8″ × 3/8″_*MP*	609.6	15.93	5.08	15.93	5.08	3.36	–
3	H_6″ × 6″ × 3/8″_*MP*	609.6	10.96	3.18	13.96	5.08	3.58	3.09

Table 4a
Experimental results for specimens of *Group 2* (H-specimens in eccentric-point loading): failure loads, displacements and linear axial stiffnesses (values in kips, in.).

#	Specimens	Length (in.)	Load (linear limit) (P_l) (kips)	δ_l (in.)	Failure load (P_f) (kips)	δ_f (in.)	Linear axial stiffness K_{jl}^A (kip/in)	Average lin. axial stiffness $\overline{K}_{jl}^A$ (kip/in)
4	H_10″ × 10″ × 1/2″_EP	24	5.73	0.44	5.73	0.44	14.38	–
5	H_8″ × 8″ × 3/8″_EP	24	3.54	0.36	3.54	0.36	9.99	–
6	H_6″ × 6″ × 3/8″_EP	24	1.89	0.15	2.85	0.30	12.29	10.87

Table 4b
Experimental results for specimens of *Group 2* (H-specimens in eccentric-point loading): failure loads, displacements and linear axial stiffnesses (values in kN, mm).

#	Specimens	Length (mm)	Load (linear limit) (P_l) (kN)	δ_l (mm)	Failure load (P_f) (kN)	δ_f (mm)	Linear axial stiffness K_{jl}^A (kN/mm)	Average lin. axial stiffness $\overline{K}_{jl}^A$ (kN/mm)
4	H_10″ × 10″ × 1/2″_EP	609.6	25.51	11.10	25.51	11.10	2.52	–
5	H_8″ × 8″ × 3/8″_EP	609.6	15.74	9.19	15.74	9.19	1.75	–
6	H_6″ × 6″ × 3/8″_EP	609.6	8.40	3.81	12.69	7.62	2.15	1.90

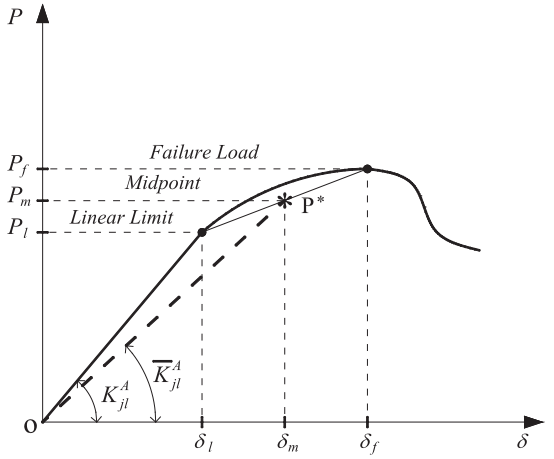

Fig. 13. Linear axial stiffness, K_{jl}^A, and average linear axial stiffness, $\overline{K}_{jl}^A$.

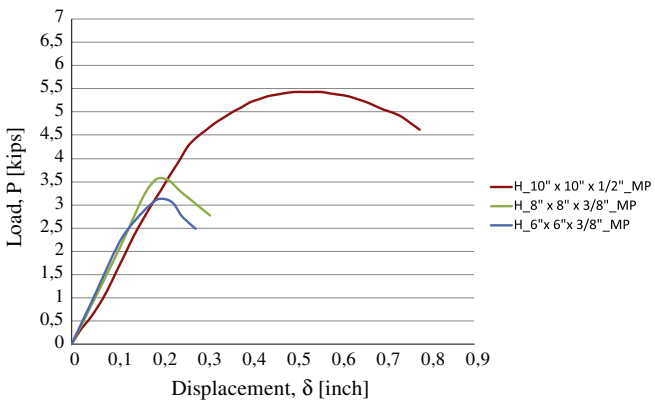

Fig. 14. Load (P) versus displacement (δ) curve for H-specimens in mid-point loading (*Group 1*).

corresponds to a load level of 4.25 kips (18.93kN). After which, a stiffness degradation was observed and the load–displacement (P–δ) behavior followed a near-linear behavior until a 0.56″ (14.22 mm) displacement level was reached corresponding to a 5.43 kips (24.15 kN) axial load. After that, signs of failure started to occur. Fig. 16 shows the load–displacement curve at mid-point. Equivalent linearized load–displacement relation measured at

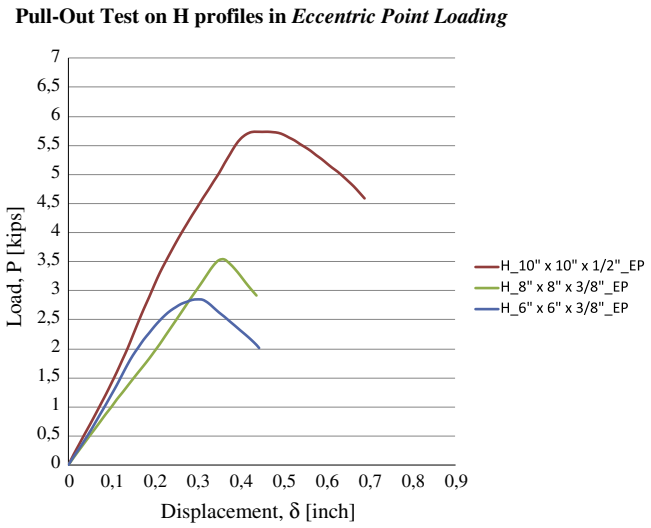

Fig. 15. Load (P) versus displacement (δ) curve for H-specimens in eccentric-point loading (*Group 2*).

specimen's mid-point is shown in Fig. 17. Fig. 18 shows the displacement pattern along the upper flange length at 1.0 kip (4.448 kN) loading steps.

– *Specimen #2* H_8″ × 8″ × 3/8″ (203.2 mm × 203.2 mm × 9.5 mm)_*MP*.

For this specimen, the P–δ behavior was similar to the previous one where linearity continued up to a displacement of 0.20″ (5.08 mm) corresponding to a pull load level of 3.58 kips (15.93 kN). Beyond this load level, signs of failure were observed leading to a complete total separation of the flange from the web that was initiated at the location of the pull load line and propagated to the rest of the junction length. Fig. 19 shows the load–displacement curve at the specimen's mid-point. Equivalent linearized P–δ relation at mid-point of this specimen is presented in Fig. 20. Fig. 21 shows the displacement pattern along the upper flange length drawn at 1.0 kip (4.448 kN) loading steps.

– *Specimen #3* H_6″ × 6″ × 3/8″ (152.4 mm × 152.4 mm × 9.5 mm)_*MP*.

The P–δ behavior of this specimen was similar to other two specimens where linearity was observed up to an axial displacement

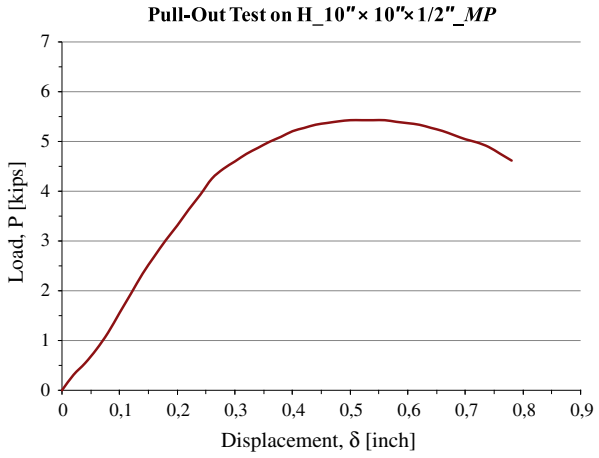

Fig. 16. Load–displacement curve for H_10″ × 10″ × ½″ (254.0 mm × 254.0 mm × 12.7 mm)_*MP* specimen at loading-point.

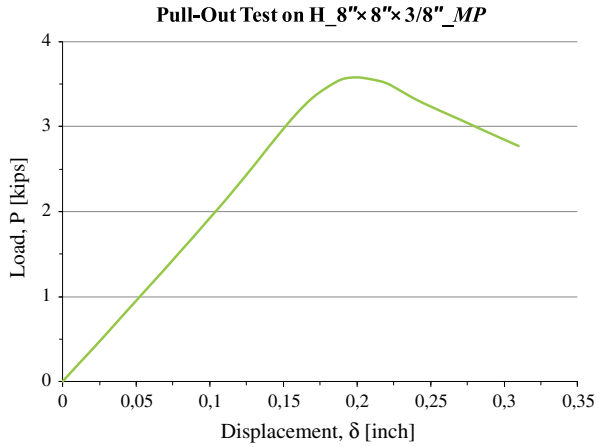

Fig. 19. Load–displacement curve for H_8″ × 8″ × 3/8″ (203.2 mm × 203.2 mm × 9.5 mm)_*MP* specimen at loading-point.

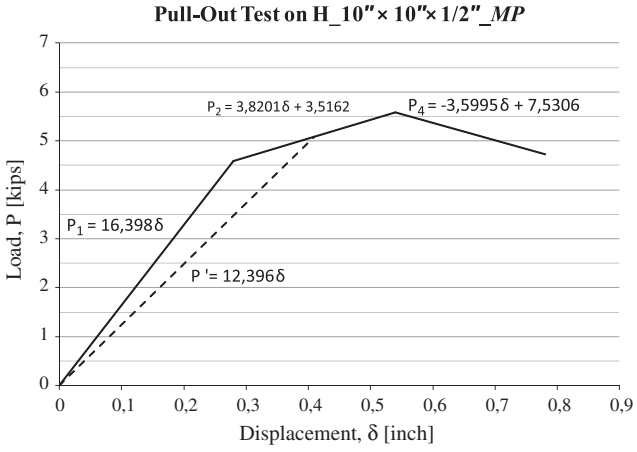

Fig. 17. Linearized load–displacement curve for H_10″ × 10″ × ½″ (254.0 mm × 254.0 mm × 12.7 mm)_*MP* specimen at loading-point.

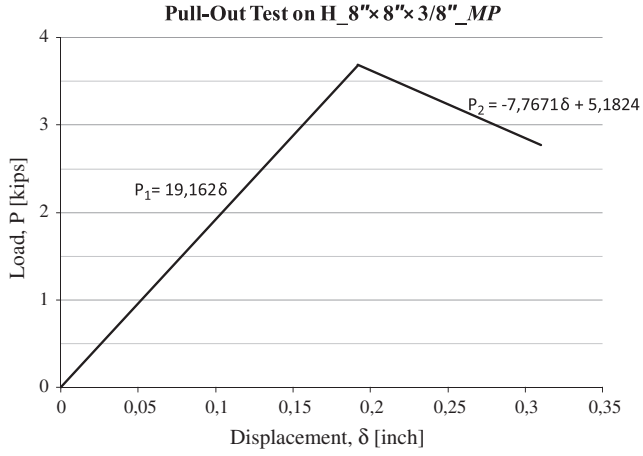

Fig. 20. Linearized load–displacement curve for H_8″ × 8″ × 3/8″ (203.2 mm × 203.2 mm × 9.5 mm)_*MP* specimen at loading-point.

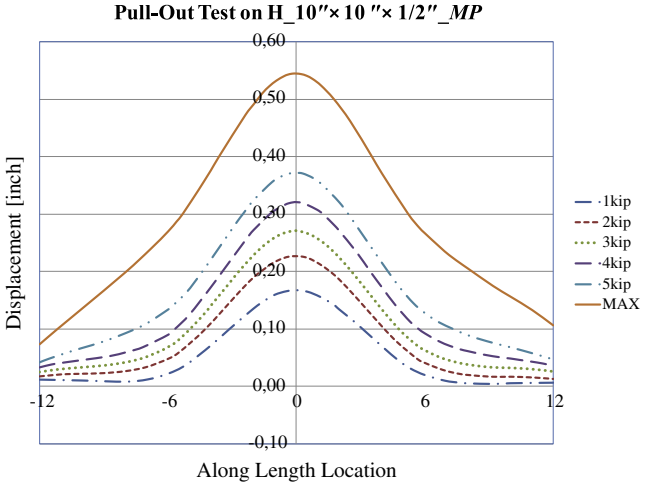

Fig. 18. Displacement pattern along upper flange length for H_10″ × 10″ × ½″ (254.0 mm × 254.0 mm × 12.7 mm)_*MP* specimen at loading-point.

level of 0.125″ (3.18 mm) corresponding to a load equal to 2.46 kips (10.96 kN). As the load increased, the stiffness degradation was observed while linear behavior was maintained up to a displacement level of 0.20″ (5.08 mm) that corresponds to a load of 3.14 kips (13.96 kN). Beyond this load level, localized junction failure was initiated. The load–displacement curve at mid-point is shown in Fig. 22, and the proposed trilinear idealized behavior is presented in Fig. 23. Fig. 24 shows the displacement pattern along the upper flange length at 1.0 kip (4.448 kN) loading steps.

5.1.2. Group 2: Eccentric-point loading tests results

– *Specimen #4* H_10″ × 10″ × ½″ (254.0 mm × 254.0 mm × 12.7 mm)_*EP*.

For this specimen, the displacement was increased linearly with increasing load up to 0.44″ (11.09 mm) displacement and 5.73 kips (25.51 kN) axial load. After which, failure started to occur. Fig. 25 shows the load–displacement curve at loading-point. Equivalent linearized load–displacement at loading-point is shown in Fig. 26. Fig. 27 shows the displacement pattern along the upper flange length at 1.0 kip (4.448 kN) loading steps.

– *Specimen #5* H_8″ × 8″ × 3/8″ (203.2 mm × 203.2 mm × 9.5 mm)_*EP*.

For this specimen, the displacement was observed increasing linearly with load until achieving a displacement equal to 0.36″ (9.19 mm) and load equal to 3.54 kips (15.74 kN). Beyond this load

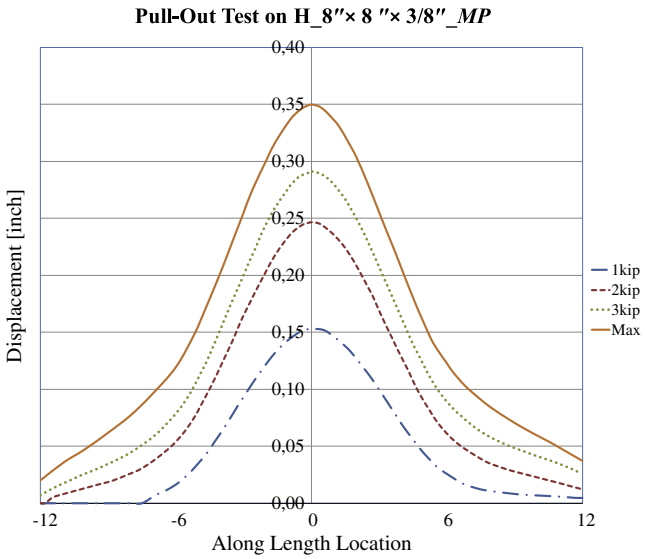

Fig. 21. Displacement pattern along upper flange length for H_8″ × 8″ × 3/8″ (203.2 mm × 203.2 mm × 9.5 mm)_*MP* specimen at loading-point.

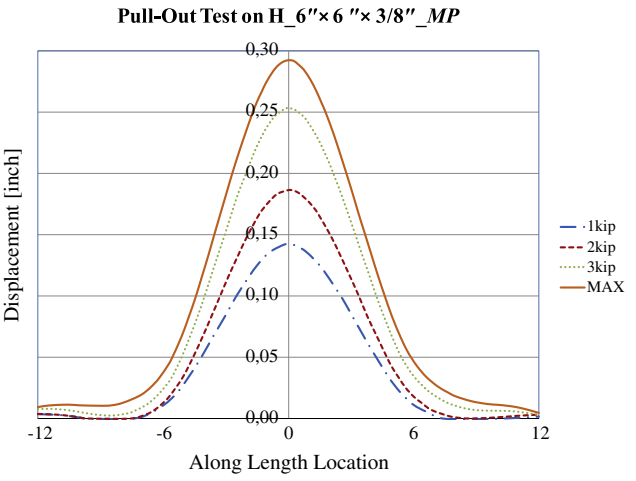

Fig. 24. Displacement pattern along upper flange length for H_6″ × 6″ × 3/8″ (152.4 mm × 152.4 mm × 9.5 mm)_*MP* specimen at loading-point.

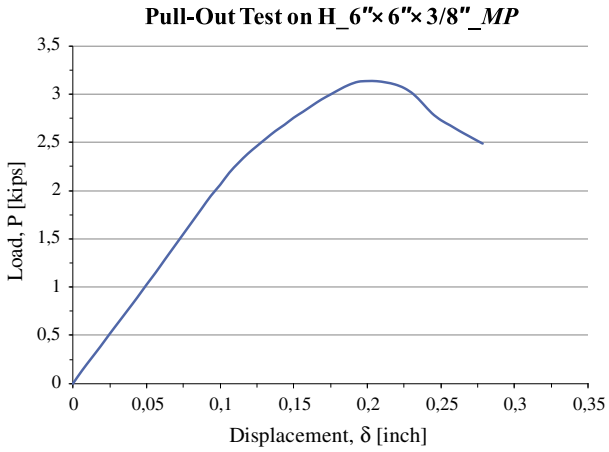

Fig. 22. Load–displacement curve for H_6″ × 6″ × 3/8″ (152.4 mm × 152.4 mm × 9.5 mm)_*MP* specimen at loading-point.

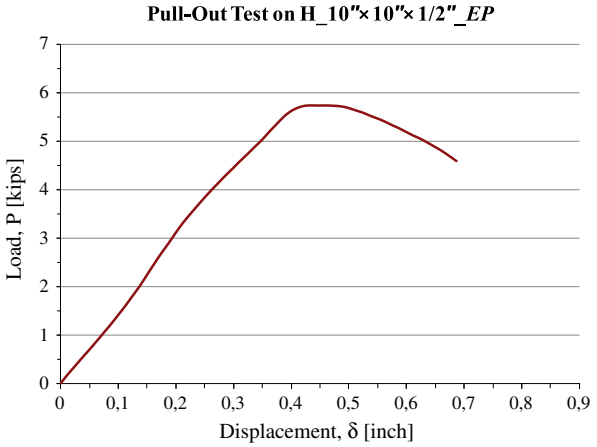

Fig. 25. Load–displacement curve for H_10″ × 10″ × ½″ (254.0 mm × 254.0 mm × 12.7 mm)_*EP* specimen at loading-point.

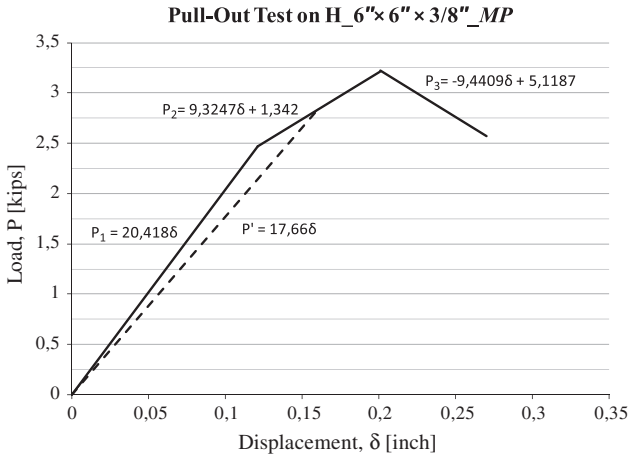

Fig. 23. Linearized load–displacement curve for H_6″ × 6″ × 3/8″ (152.4 mm × 152.4 mm × 9.5 mm)_*MP* specimen at loading-point.

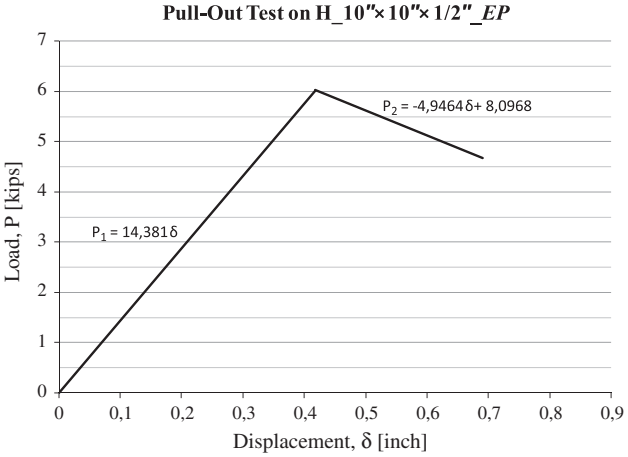

Fig. 26. Linearized load–displacement curve for H_10″ × 10″ × ½″ (254.0 mm × 254.0 mm × 12.7 mm)_*EP* specimen at loading-point.

level, localized junction cracks were observed. Fig. 28 shows the load–displacement curve at loading-point while Fig. 29 shows the equivalent linearized load–displacement at loading-point.

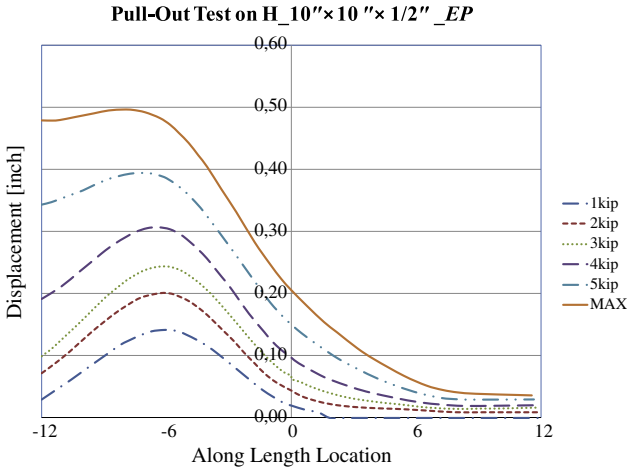

Fig. 27. Displacement pattern along upper flange length for H_10″ × 10″ × ½″ (254.0 mm × 254.0 mm × 12.7 mm)_*EP* specimen at loading-point.

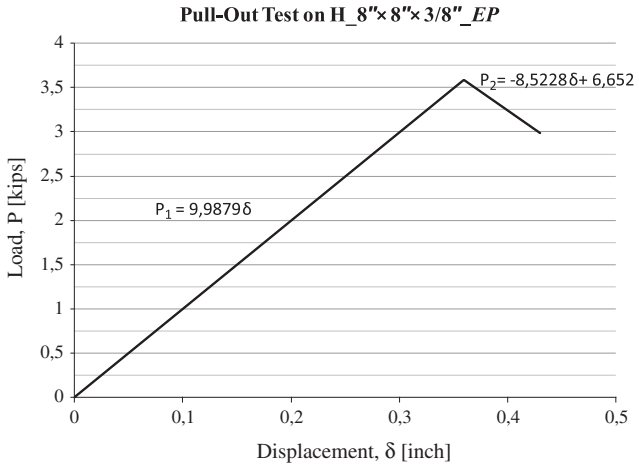

Fig. 29. Linearized load–displacement curve for H_8″ × 8″ × 3/8″ (203.2 mm × 203.2 mm × 9.5 mm)_*EP* specimen at loading-point.

Displacement pattern along the upper flange length at 1.0 kip (4.448 kN) loading steps is shown in Fig. 30.

– *Specimen #6* H_6″ × 6″ × 3/8″ (152.4 mm × 152.4 mm × 9.5 mm)_*EP*.

For this specimen, the displacement and the load was linearly proportional up to a displacement equal to 0.15″ (3.81 mm) and load equal to 1.88 kips (8.40 kN). As the load increased, stiffness degraded even though the P–δ relation remained linear up to 0.3″ (7.62 mm) displacement that corresponds to a load of 2.85 kips (12.69 kN). After this load level, local failure started to occur. The load–displacement curve at loading-point is shown in Fig. 31, and the equivalent linearized curve is shown in Fig. 32. Fig. 33 shows the displacement pattern along the upper flange length at 1.0 kip (4.448 kN) loading steps.

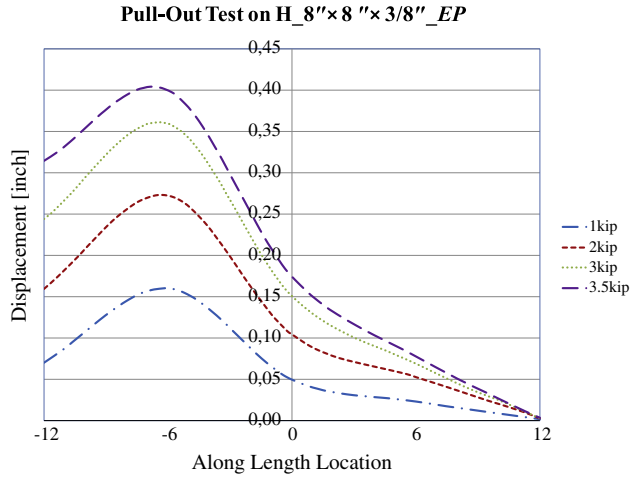

Fig. 30. Displacement pattern along upper flange length for H_8″ × 8″ × 3/8″ (203.2 mm × 203.2 mm × 9.5 mm)_*EP* specimen at loading-point.

5.2. Relative rotation test results

The main experimental results obtained from the relative rotations tests are summarized in Table 5. Fig. 34 presents the moment–rotation (M–θ) curves for all three pultruded H-profile specimens while Figs. 35 and 36 show the M–θ curves for the two pultruded L-profile specimens in both open-mode (*R_OM*)

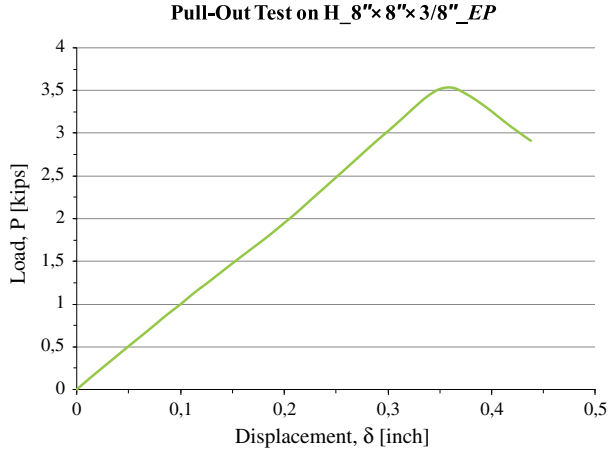

Fig. 28. Load–displacement curve for H_8″ × 8″ × 3/8″ (203.2 mm × 203.2 mm × 9.5 mm)_*EP* specimen at loading-point.

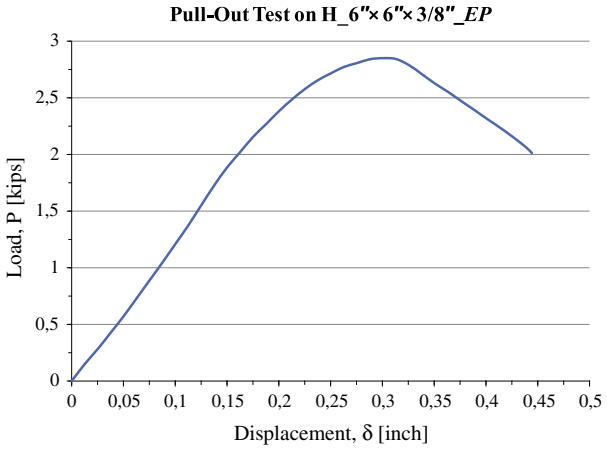

Fig. 31. Load–displacement curve for H_6″ × 6″ × 3/8″(152.4 mm × 152.4 mm × 9.5 mm)_*EP* specimen at loading-point.

and close-mode (*R_CM*), respectively. It should be noted, in a typical semi-rigid framing connection such that shown in Fig. 1, both opening mode (top clip angle) and closing mode (bottom clip seat

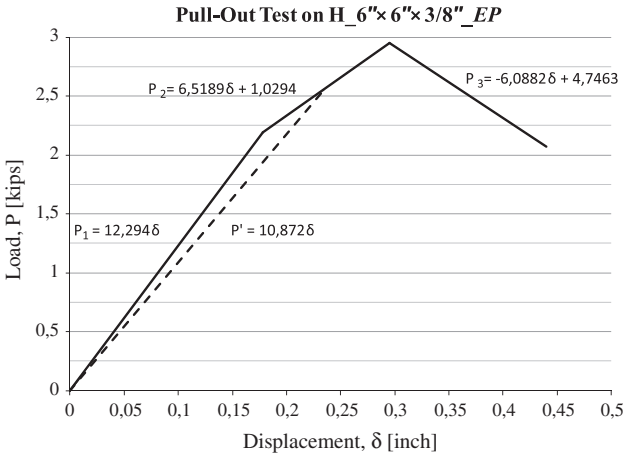

Fig. 32. Linearized load–displacement curve for H_6″ × 6″ × 3/8″ (152.4 mm × 152.4 mm × 9.5 mm)_*EP* specimen at loading-point.

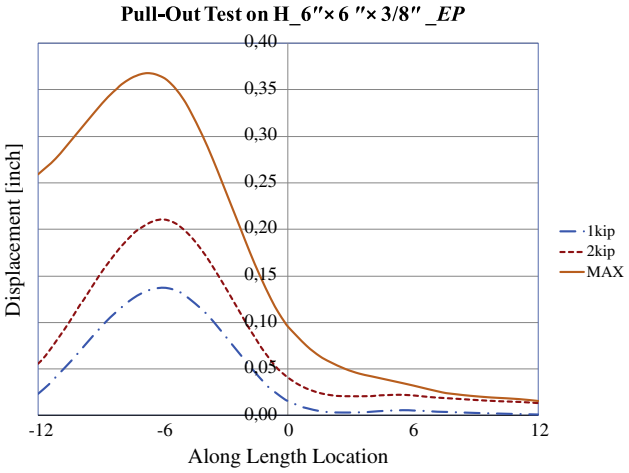

Fig. 33. displacement pattern along upper flange length for H_6″ × 6″ × 3/8″ (152.4 mm × 152.4 mm × 9.5 mm)_*EP* specimen at loading-point.

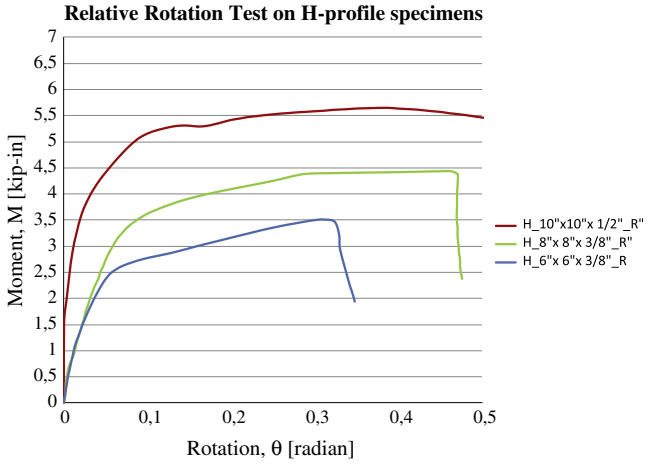

Fig. 34. Moment–rotation (M–θ) curves for H-profile specimens in relative rotation test.

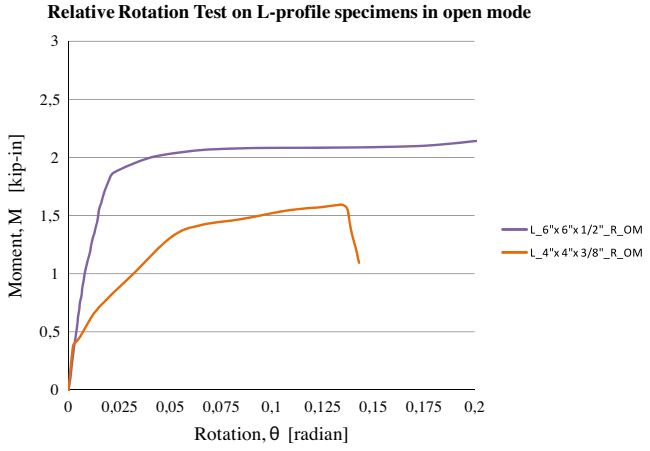

Fig. 35. Moment–rotation (M–θ) curves for open mode L-profile specimens in relative rotation test.

angle) will potentially suffer local damages even when gravity loads are applied. This local damage will be amplified when the connection is exposed to cyclic loadings [35].

– *Specimen #7* H_10″ × 10″ × ½″ (254.0 mm × 254.0 mm × 12.7 mm)_*R*.

For this specimen, it was observed that the rotation was very small up to moment less or equal to 1.5 kip.in (169.5 kN mm). The relation between moment and rotation angle remained linear up to 3.56 kip.in (402.65 kN mm) moment and 0.02 radian rotation angle. After that level degradation in the stiffness started to occur, even though the relation between moment and rotation stayed linear up to 5.22 kip.in (589.79 kN mm) moment and 0.11 radian rotation angle. From here, large increases in rotation angle were observed with very small changes in moment up to 0.4 radian rotation angle. After this point, failure started to occur (Fig. 37). Fig. 38 shows the moment–rotation curve for the H-profile, while the linearized curve is shown in Fig. 39.

– *Specimen #8* H_8″ × 8″ × 3/8″ (203.2 mm × 203.2 mm × 9.5 mm)_*R*.

For this specimen, it was observed that the rotation was very small up to moment equal to 0.7 kip.in (79.1 kN mm). Beyond this

Table 5
Relative rotation test experimental results for H and L-profile specimens.

#	Specimens	Length (mm)	(in.)	Moment (linear limit) (M_l) (kN mm)	(kip.in)	θ_l (rad)	Failure moment (M_f) (kN mm)	(kip.in)	θ_f (rad)	θ_u (rad)
7	H_10″ × 10″ × 1/2″_*R*	152.4	6.00	402.65	3.56	0.02	589.79	5.22	0.11	0.40
8	H_8″ × 8″ × 3/8″_*R*	152.4	6.00	409.73	3.63	0.10	497.09	4.40	0.30	0.46
9	H_8″ × 8″ × 3/8″_*R*	152.4	6.00	296.70	2.63	0.07	395.62	3.50	0.30	–
10	L_6″ × 6″ × 1/2″_*R_OM*	152.4	6.00	209.16	1.85	0.02	209.16	1.85	0.02	0.40
11	L_6″ × 6″ × 1/2″_*R_CM*	152.4	6.00	985.46	8.72	0.14	985.46	8.72	0.14	–
12	L_4″ × 4″ × 3/8″_*R_OM*	152.4	6.00	147.47	1.30	0.05	147.47	1.30	0.05	0.13
13	L_4″ × 4″ × 3/8″_*R_CM*	152.4	6.00	482.21	4.27	0.15	482.21	4.27	0.15	–

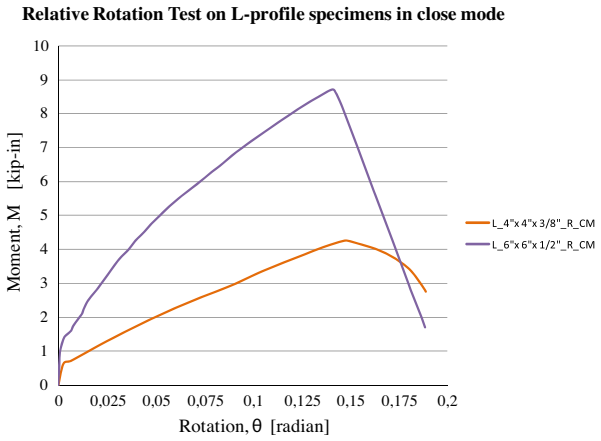

Fig. 36. Moment–rotation (M–θ) curves for close mode L-profile specimens in relative rotation test.

point, the relation between moment and rotation angle remained linear up to 3.62 kip.in (409.73 kN mm) moment and 0.10 radian rotation angle. After this point, stiffness degradation was observed; however, the relation between moment and rotation (M–θ) remained linear up to 4.40 kip.in (497.09 kN mm) moment and 0.3 radian rotation angle. In the final leg, increasing in rotation angle was observed without any change in moment up to 0.46 radian rotation angle, after that the failure suddenly occurred (Fig. 40). Fig. 41 shows the M–θ curve for 8″ × 8″ × 3/8″ (203.2 mm × 203.2 mm × 9.5 mm) H-profile, while the linearized curve is shown in Fig. 42.

– *Specimen #9* H_6″ × 6″ × 3/8″ (152.4 mm × 152.4 mm × 9.5 mm)_*R*.

For this specimen, identical behavior was noticed. The rotation was very small up to moment equal to 0.7 kip.in (79.1 kN mm); after which, the relation between moment and rotation angle was linear up to 2.63 kip.in (296.70 kN mm) moment and 0.07 radian rotation angle. Beyond this point degradation in the stiffness started to occur but the relation between moment and rotation remained linear up to 3.50 kip.in (395.62 kN mm) moment and 0.30 radian rotation angle, at which time failure occurred (Fig. 43). Fig. 44 shows the moment–rotation curve for the 6″ × 6″ × 3/8″ H-profile, while the linearized curve is shown in Fig. 45.

– *Specimen #10* L_6″ × 6″ × ½″ (152.4 mm × 152.4 mm × 12.7 mm)_*R_OM*.

For the L-specimen in open mode, it was observed that the rotation was very small up to a moment equal to 1.0 kip.in

Fig. 37. Failure of 10″ × 10″ × ½″ (254.0 mm × 254.0 mm × 12.7 mm) H-profile.

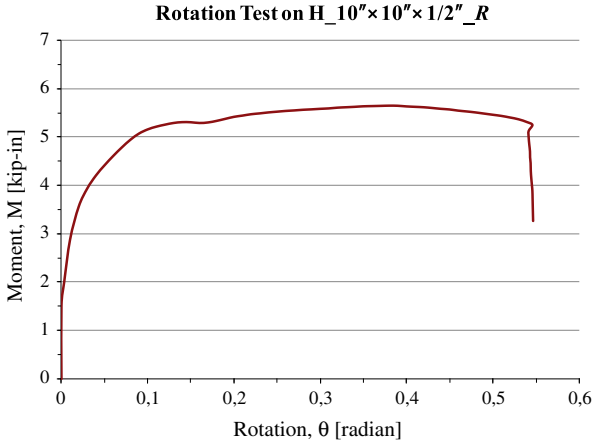

Fig. 38. Moment–rotation curve for H_10″ × 10″ × ½″ (254.0 mm × 254.0 mm × 12.7 mm)_*R* specimen.

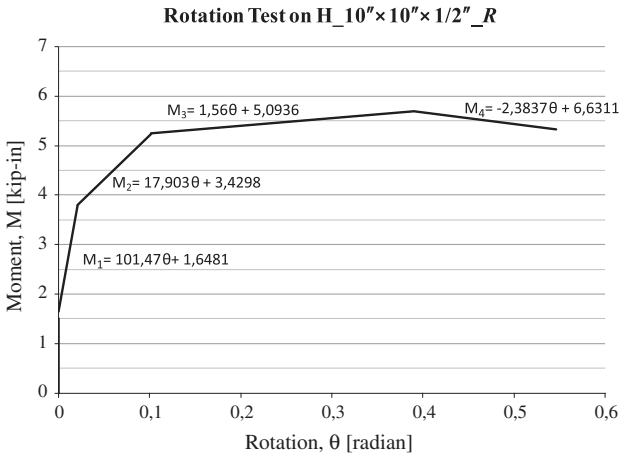

Fig. 39. Linearized moment–rotation curve for H_10″ × 10″ × ½″ (254.0 mm × 254.0 mm × 12.7 mm)_*R* specimen.

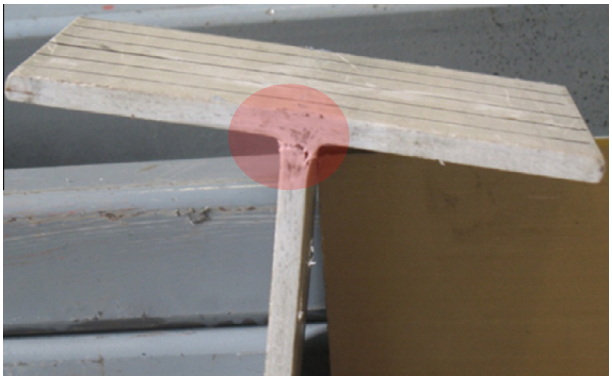

Fig. 40. Failure of H_8″ × 8″ × 3/8″ (203.2 mm × 203.2 mm × 9.5 mm)_*R* specimen.

(113.03 kN mm); after that the relation between moment and rotation angle was linear up to 1.85 kip.in (209.16 kN mm) moment and a rotational angle of 0.02 radian. Increases in rotation angle were observed with small increases in moment till 0.40 radian rotation angle was reached, after which, ultimate local junction (corner) failure occurs suddenly (refer to Fig. 46). Fig. 47 shows the moment–rotation (M–θ) curve for open-mode loading of 6″ × 6″ × ½″ (152.4 mm × 152.4 mm × 12.7 mm) L-profile, while

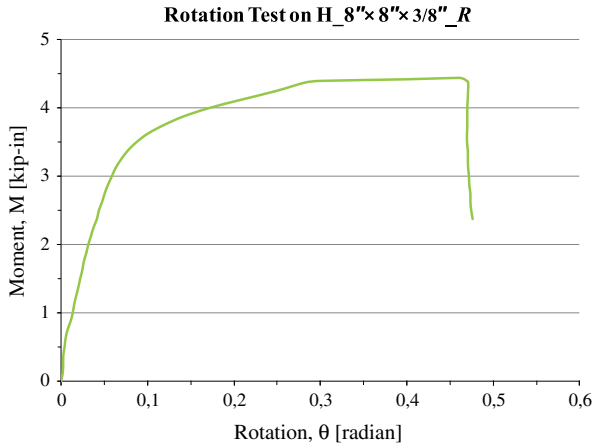

Fig. 41. Moment–rotation curve for H_8″ × 8″ × 3/8″ (203.2 mm × 203.2 mm × 9.5 mm)_*R* specimen.

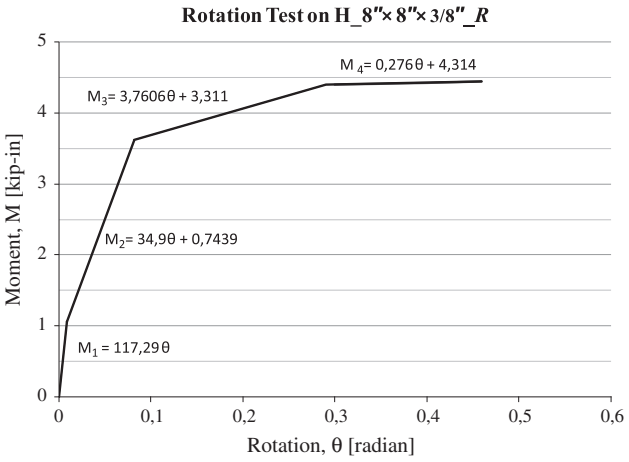

Fig. 42. Linearized moment–rotation curve for H_8″ × 8″ × 3/8″ (203.2 mm × 203.2 mm × 9.5 mm)_*R* specimen.

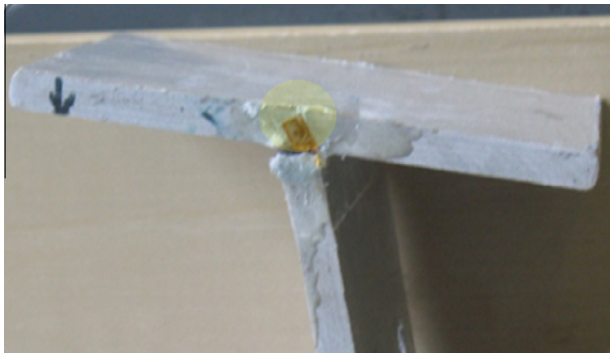

Fig. 43. Failure of H_6″ × 6″ × 3/8″ (152.4 mm × 152.4 mm × 9.5 mm)_*R* specimen.

the idealized bi-linear curve is presented in Fig. 48. It should be noted that the damage in the open mode is due to the development of interlaminar cracks that are initiated by the action of the radial stress components (especially at the higher stresses developed at the inner side of the angle's corner) due to the negligible through-the-thickness strength of pultruded composites (Fig. 46).

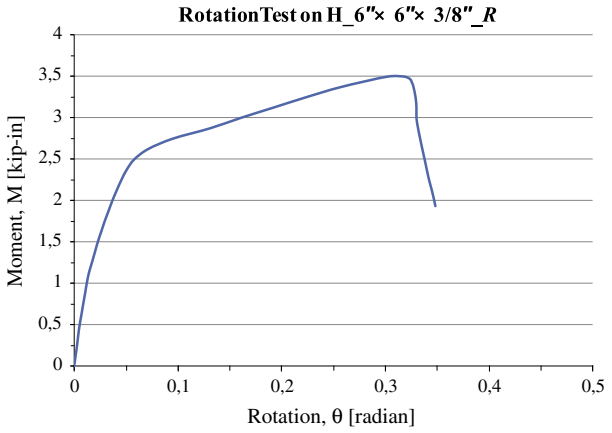

Fig. 44. Moment–rotation curve for H_6″ × 6″ × 3/8″ (152.4 mm × 152.4 mm × 9.5 mm)_*R* specimen.

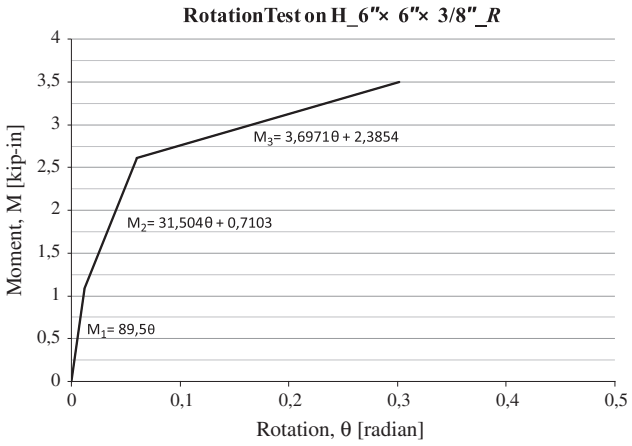

Fig. 45. Linearized moment–rotation curve for H_6″ × 6″ × 3/8″ (152.4 mm × 152.4 mm × 9.5 mm)_*R* specimen.

– *Specimen #11* L_6″ × 6″ × ½″(152.4 mm × 152.4 mm × 12.7 mm)_*R_CM.*

For the L-specimen in close mode, it was observed that the rotation was very small up to moment equal to 1.00 kip.in (113.03 kN mm), after that the relation between moment and rotation angle was linear up to 8.72 kip.in (985.46 kN mm) moment and 0.14 radian rotation angle. After that the failure started to occur (Fig. 46). Fig. 49 shows the M–θ curve for close mode of 6″ × 6″ × ½″ (152.4 mm × 152.4 mm × 12.7 mm) L-profile, while the linearized curve is shown in Fig. 50. As shown in Fig. 46, the strength of the pultruded angle was controlled by both local buckling at the inner side of the angle corner and the matrix tensile rupture at the exterior side of the angle corner.

– *Specimen #12* L_4″ × 4″ × 3/8″(101.6 mm × 101.6 mm × 9.5 mm)_*R_OM.*

For this specimen in open mode, it was observed that the rotation was very small up to a moment equal to 0.4 kip.in (45.21 kN mm). The relation between moment and rotation angle was linear up to 1.30 kip.in (147.47 kN mm) moment and 0.05 radian rotation angle. After that, increases in rotation angle were observed with small increases in moment till 0.13 radian rotation angle. After this point, the failure suddenly occurred (Fig. 46). Fig. 51 shows the moment–rotation curve for open mode of 4″ × 4″ × 3/8″ (101.6 mm × 101.6 mm × 9.5 mm) L-profile, while the linearized curve is shown in Fig. 52.

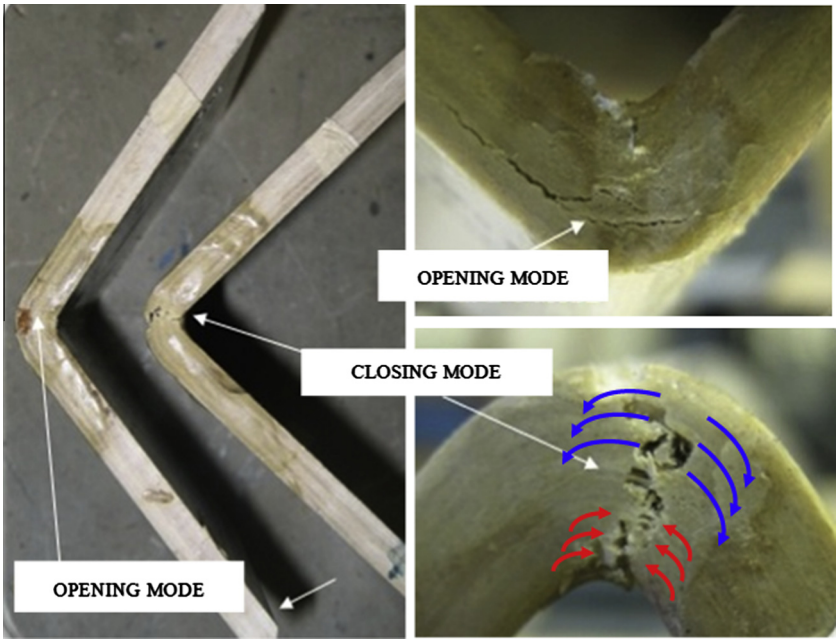

Fig. 46. Failure of L-profile specimens, *opening* and *closing mode*.

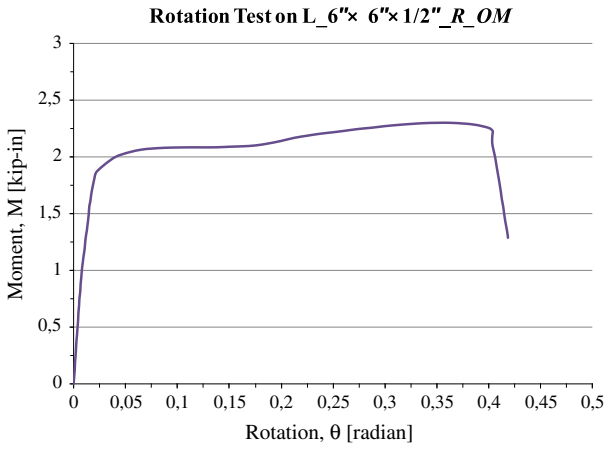

Fig. 47. Moment–rotation curve for L_6″ × 6″ × ½″ (152.4 mm × 152.4 mm × 12.7 mm)_*R_OM* specimen.

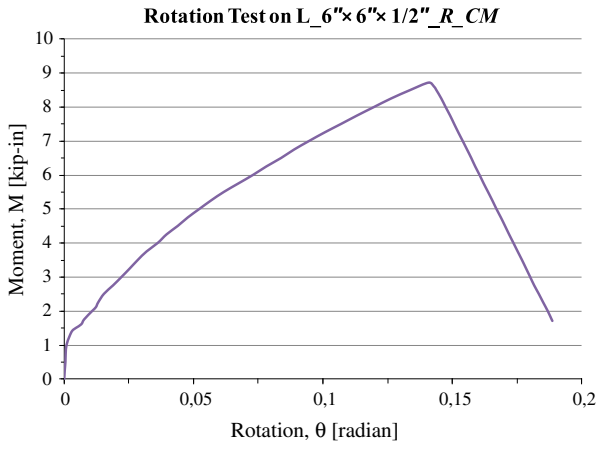

Fig. 49. Moment–rotation curve for L_6″ × 6″ × ½″ (152.4 mm × 152.4 mm × 12.7 mm)_*R_CM* specimen.

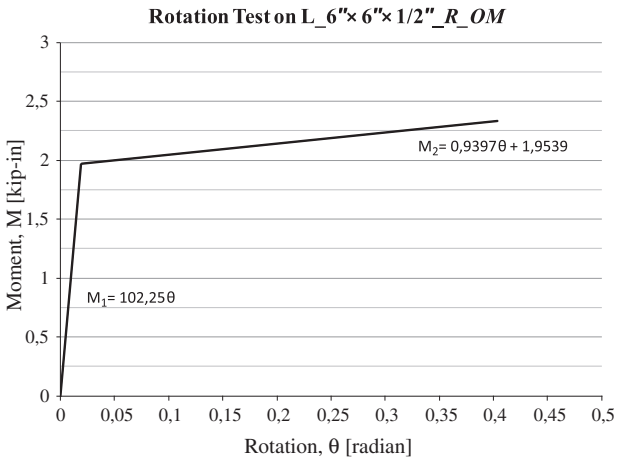

Fig. 48. Linearized moment–rotation curve for L_6″ × 6″ × ½″ (152.4 mm × 152.4 mm × 12.7 mm)_*R_OM* specimen.

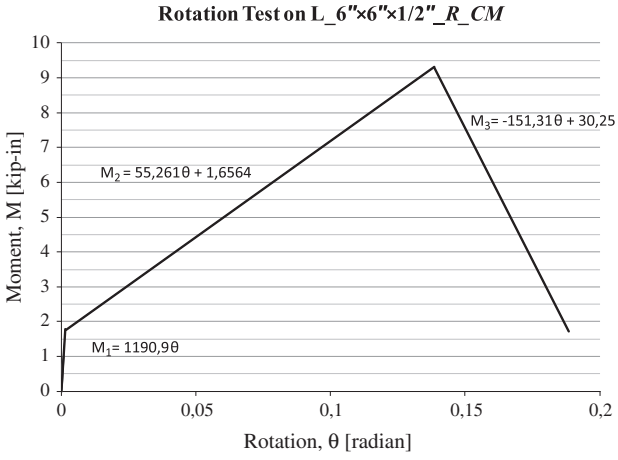

Fig. 50. Linearized moment–rotation curve for L_6″ × 6″ × ½″ (152.4 mm × 152.4 mm × 12.7 mm)_*R_CM* specimen.

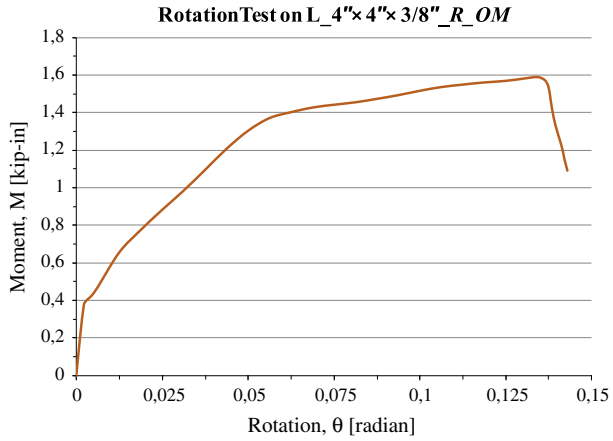

Fig. 51. Moment–rotation curve for L_4″ × 4″ × 3/8″ (101.6 mm × 101.6 mm × 9.5 mm)_*R_OM* specimen.

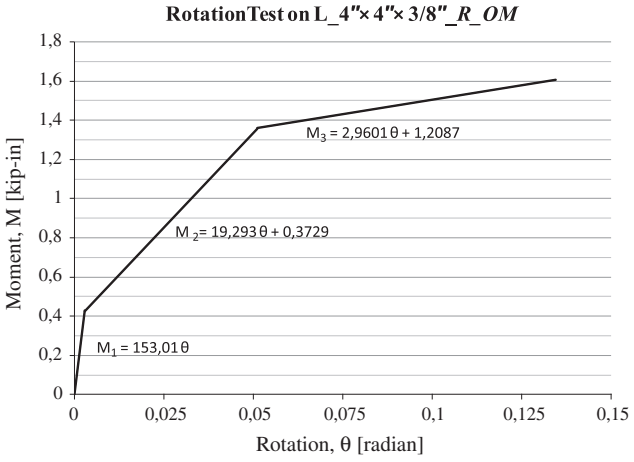

Fig. 52. Linearized moment–rotation curve for L_4″ × 4″ × 3/8″ (101.6 mm × 101.6 mm × 9.5 mm)_*R_OM* specimen.

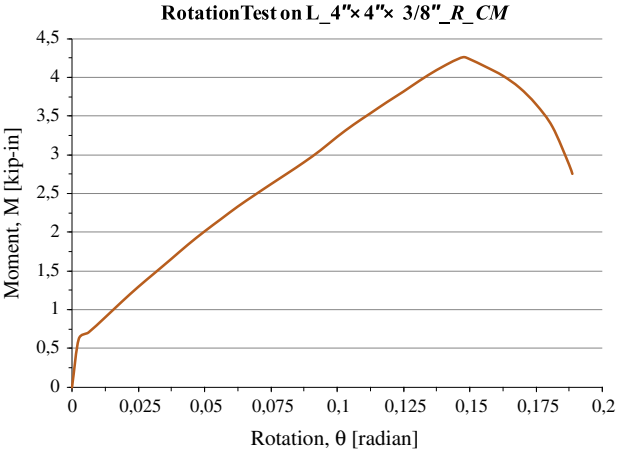

Fig. 53. Moment–rotation curve for L_4″ × 4″ × 3/8″ (101.6 mm × 101.6 mm × 9.5 mm)_*R_CM* specimen.

– *Specimen #13* L_4″ × 4″ × 3/8″ (101.6 mm × 101.6 mm × 9.5 mm)_*R_CM*.

For this specimen in close mode, it was observed that the rotation was very small up to a moment equal to 0.71 kip.in (80.5 kN mm). The relation between moment and rotation angle

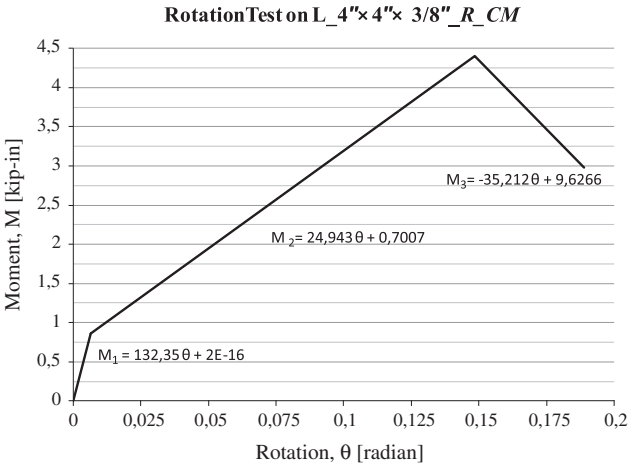

Fig. 54. Linearized moment–rotation curve for L_4″ × 4″ × 3/8″ (101.6 mm × 101.6 mm × 9.5 mm)_*R_CM* specimen.

remained linear up to 4.27 kip.in (482.21 kN mm) moment and 0.15 radian rotation angle. After that the failure started to occur (Fig. 46). Fig. 53 shows the moment–rotation curve for close mode of 4″ × 4″ × 3/8″ L-profile, while the linearized curve is shown in Fig. 54.

6. Conclusions and recommendations

The aim of the experimental investigation presented in this paper was to provide technical information on one of the structural deficiencies and behavioral limitations related to the weak junction between the web and flange of commercially produced, off-the-shelf unidirectional pultruded composites.

In particular, this work presents the experimental results of the second phase of a multi-phase comprehensive joint research program between University of Salerno, Italy and the University of California, Irvine, USA on investigating one of the major structural issues that defines a critical strength limit-state that can determine the feasibility and the reliability of using PFRP composite profiles as primary members.

With this aim, six pull-out tests and seven relative rotation tests were performed on the web–flange junctions of three different sizes of PFRP pultruded H-profiles and two different sizes of L-profiles in order to evaluate both the axial and the rotational stiffness and strength of such junctions. In conducting this experimental investigation, special test fixtures were designed, fabricated and verified through different tests. The following conclusions are drawn from the results of this study:

(i) The orthotropic and viscoelastic behavior of the PFRP sections must be taken into consideration when designing PFRP structural members.

(ii) Local failure of web/flange junction of unidirectional pultruded profiles influences both stiffness and strength limit-states of pultruded structures. For this reason, web/flange junction strength should be included in all design equations, codes, specifications and standards to ensure reliability and serviceability of pultruded composite structures. Until this weakness is mitigated by the pultrusion industry, stiffened and strengthening details must be adopted in all design of PFRP structures. This issue is discussed in details by Mosallam [36]. Chapter 7 of the American Society of Civil Engineers (ASCE) Design Manual MOP 102 [11] provides a varity of strengthening details for open and close-web pultruded composite profiles as well as different connection details.

(iii) Due to the inherent flexibility of the junction between web and flanges of open-web pultruded profiles, this junction should be modeled as an axial spring or rotational spring depending on the nature of applied loads. For example, unlike steel open-web profiles, a rotational spring, replacing the WFJ should be used for accurate effective stiffness characterization used in analyzing buckling, post-buckling and torsional behavior of pultruded beams and columns. For realistic modeling, experimental non-linear or linearized rotational/axial stiffness expressions should be used for simulating the behavior of PFRP members. Examples of such expressions are presented in this paper.

(iv) Experimental results indicated that PFRP L-profiles exhibit different behaviors in open- and close-modes. For example, the close-mode strength of the angle size is 3–4 times the open-mode strength of the pultruded angle profile. It should be noted that the damage in the open mode is due to the development of interlaminar cracks that are initiated by the action of the radial stress components due to the negligible through-the-thickness strength of pultruded composites. However, in the close-mode, the strength of the pultruded angle is controlled by both local buckling at the inner side of the angle corner and the matrix tensile rupture at the exterior side of the angle corner as illustrated in Fig. 46. In both modes, the fibers are running in orthogonal direction (wrong direction) to the applied load that is resisted mainly by the weak polymeric matrix. This L-profile is commonly used as a connecting element for different connection details, including: beam-column, beam-girder and column-base connections for PFRP structures. This difference in both stiffness and strength should be considered in designing such connections under both static and dynamic loads.

(v) This study highlighted the importance of the junction strength and stiffness and its influence on overall structural behavior of pultruded composte structures. For this reason, it is necessary to develop a set of ASTM or/and ISO standard tests to provide the designers with the necessary strength and stiffness information that will establish the design limit states for pultruded composites structures. In this phase of the multi-phase research study, a simple, yet effective test fixtures were designed, fabricated and implemented. These fixture can be a foundation for tests standards for WFJ of pultruded composite open-web profiles.

It is hoped that the results of this multi-phase research program will fill the exisiting gaps and will provide structural engineers with essential engineering data to assist to secure optimum designs and obtain the maximum benefit of PFRP materials.

References

[1] Mosallam AS. Chapter on composites in construction. In: Materials selection handbook. John Wiley Publishing Co; 2002 [chapter 45].

[2] Bank LC. Composites for construction: structural design with FRP materials. John Wiley & Sons; 2006.

[3] Mosallam AS. Durability of pultruded fiber reinforced polymer (PFRP) composites in mining environments. In: Benmokrane B, Rahman H, editors. Durability of fiber reinforced polymer (FRP) composites for construction. Canada: University of Sherbrooke; 1998. p. 649–59.

[4] Mosallam AS, Feng M, Nasr A. Non-destructive evaluation of fiber reinforced polymer (FRP) composite bridge decks – Part II, A Final Report, Report # SETH-Caltrans-NDE1009, Submitted to California Department of Transportation (CalTrans); October 2009. 50pps.

[5] Kollár LP, Springer GS. Mechanics of composites structures. Cambridge University Press; 2003.

[6] Ascione L, Feo L. Mechanical behavior of composites for construction. In: Wiley encyclopedia of composites. John Wiley & Sons; 2012. p. 1625–49. 2nd Edition, 2.

[7] Barbero EJ. Introduction to composite material design. Philadelphia: Taylor & Francis; 1998.

[8] Eurocomp Design Code and Handbook, Structural design of polymer composites. The European Structural Polymeric Composites Group; 1996. (ISBN 0419194509).

[9] European Committee for Standardization (CEN). EN 13706: Reinforced plastics composites – Specifications for pultruded profiles. Part 1: Designation; Part 2: Methods of test and general requirements; Part 3: Specific requirements, Brussels: CEN; 2002.

[10] Technical Document CNR-DT 205/2007. Guide for the design and construction of structures made of FRP pultruded elements. Italian National Research Council (CNR) Rome; 2008.

[11] Mosallam AS. Design guide for FRP composite connections. Manuals of Practice (MOP) 102. American Society of Civil Engineers (ASCE); 2011. ISBN: 9780784406120: 624.

[12] Technical Document CNR-DT 205/2007. Guide for the design and construction of structures made of FRP pultruded elements. Rome: Italian National Research Council (CNR); 2008.

[13] Davalos JF, Salim HA, Qiao P, Lopez-Andio R. Analysis and design of pultruded FRP shapes under bending. Compos B Eng 1996;27B(3,4):295–305.

[14] Mosallam AS, Abdelhamid MK, Conway JH. Performance of pultruded FRP connection under static and dynamic loads. J Reinforced Plast Compos 1996;13:1052–67.

[15] Mosallam AS, Abdelhamid MK. Dynamic behavior of PFRP structural Sections. In: Proc. of ASME (Energy Sources Tech. Conf. and Expo, Composite Material Tech.), 53; 1993. p. 37–44.

[16] Mosallam AS, Bank LC. Short-term behavior of pultruded fiber reinforced plastic frame. J Struct Eng (ASCE) 1992;118(7):1037–954.

[17] Liu X, Mosallam AS, Kreiner J. A numerical investigation on static behavior of pultruded composite (PFRP) portal frame structures. In: Proceeding of the 43rd international SAMPE symposium and exhibition, Anaheim, California; 1998.

[18] Bank LC, Nadipelli M, Gentry TR. Local buckling and failure of pultruded fiber-reinforced plastic beams. J Eng Mater Technol 1994;116:223–37.

[19] Bank LC, Yin J. Failure of web–flange junction on postbuckled pultruded I-beams. J Compos Constr 1999;177:177–84.

[20] Turvey GJ, Zhang Y. A computational and experimental analysis of the buckling, postbuckling and initial failure of pultruded GRP columns. Compos Struct 2006;84:1527–37.

[21] Mosallam AS. Plastics composites for FRP 21st century construction: pultruded structural shapes. ASCE (NY); 1993 [chapter 3].

[22] Correia JR, Branco FA, Silva NMF, Camotim D, Silvestre N. First-order, buckling and post-buckling behaviour of GFRP pultruded beams. Part 1: Experimental study. Comput Struct 2011;89:2052–64.

[23] Turvey GJ, Zhang Y. Tearing failure of web–flange junctions in pultruded GRP profiles. Compos A Appl Sci Manuf 2005;36:309–17.

[24] Turvey GJ, Zhang Y. Characterisation of the rotational stiffness and strength of web–flange junctions of pultruded GRP WF-sections via web bending tests. Compos A Appl Sci Manuf 2006;37:152–64.

[25] Turvey GJ, Zhang Y. Shear failure strength of web–flange junctions in pultruded GRP WF profiles. Constr Build Mater 2006;20:81–9.

[26] Borowicz DT, Bank LC. Behavior of pultruded fiber-reinforced polymer beams subjected to concentrated loads in the plane of the web. J Compos Constr 2011;15:229–38.

[27] Leung CKY, Jiang Y, Ng MYM. A fiber-optics based technique for delamination detection at the web/flange junction of GFRP I-beams. In: Fourth international conference on FRP composites in civil engineering (CICE2008), Zurich, Switzerland, July; 2008. p. 1–6.

[28] Feo L, Mosallam AS, Penna R. Mechanical behavior of web–flange junctions of thin walled pultruded I-profiles: an experimental and numerical evaluation. Compos B Eng 2013;48:18–39.

[29] Feo L, Mosallam AS, Penna R. Preliminary results of an experimental and computational analysis of the behaviour of web–flange junctions of GFRP pultruded profiles subjected to concentrated loads. In: Proceeding of the 15th European conference on composites materials (ECCM15), Venice; 2012.

[30] Feo L, Mosallam AS, Penna R. An experimental investigation on the behavior of web–flange junctions of GRP pultruded profiles. In: Proceeding of the ICCE–20 (20th Annual International Conference on Composites/Nano Engineering), Beijing; 2012.

[31] Feo L, Penna R. On the behavior of web–flange junctions of GRP pultruded profiles. In: Proceedings of riga technical university 53rd international scientific conference dedicated to the 150th anniversary and 1st congress of world engineers and riga polytechnical institute/RTU Alumni. Riga (Latvija); 2012.

[32] Feo L, Mosallam AS, Penna R. Experimental and numerical results on the failure strength of web–flange junctions of thin walled pultruded composites profiles. In: Proceeding of the Italian association for stress analysis (AIAS) Conference, Salerno (Italy); 2013.

[33] Bedford Reinforced Plastics Design Guide, <http://bedfordreinforced.com/wp-content/uploads/2013/09/BRPDesignGuide-2012.pdf>, Bedford, PA, USA; 2012.

[34] Hassan NK, Mosallam AS. Buckling and ultimate failure of thin-walled pultruded composite columns. J Polym Polym Compos 2004;12(6):469–81.

[35] Mosallam AS, Schmitz HG. Experimental investigation on the behavior of UC beam-to-column composite connections under cyclic and sustained loads. In: Proceedings of the first international conference on composites in infrastructures (ICCI'96), University of Arizona, Tucson, Arizona, January 15–17; 1996. p. 638–50.

[36] Mosallam AS. Connections and reinforcements design details for PFRP composite structures. J Reinf Plast Compos 1996;14(July):752–84.